# Investigation of Heat Transfer across a Nanoscale Air Gap Between a Flying Head and a Rotating Disk

S. Sakhalkar,[1, a)] Q. Cheng,[1] A. Ghafari,[1] and D. Bogy[1]
*University of California at Berkeley, Berkeley, California 94720, USA*

(Dated: 28 July 2020)

Understanding nanoscale heat transfer at the head-disk interface (HDI) is necessary for thermal management of hard disk drives (HDDs), especially for Heat-Assisted Magnetic Recording and Microwave-Assisted Magnetic Recording. To accurately model the head temperature profile in HDDs, it is imperative to employ a spacing-dependent heat transfer coefficient due to the combined effects of pressurized air conduction and wave-based phonon conduction. Moreover, while flying at near-contact, the fly height and heat transfer are affected by adhesion/contact forces in the HDI. In this study, we develop a numerical model to predict the temperature profile and the fly height for a flying slider over a rotating disk. We compare our simulations with touchdown experiments performed with a flying Thermal Fly-Height Control (TFC) slider with a near-surface Embedded Contact Sensor (ECS), which helps us detect the temperature change. We incorporate the effects of disk temperature rise, adhesion/contact forces, air & phonon conduction heat transfer and friction heating in our model. As the head approaches the disk with increasing TFC power, enhanced nanoscale heat transfer leads to a drop in the ECS temperature change vs. TFC power curve. We find that the exclusion of the disk temperature rise causes the simulation to overestimate the ECS cooling drop. The incorporation of adhesion force results in a steeper ECS cooling drop. The addition of phonon conduction in the model causes a larger ECS cooling drop. The simulation with friction heating predicts a larger ECS temperature slope beyond contact. The simulation with these features agrees with the experiment.

## I. INTRODUCTION

Understanding nanoscale heat transfer between two bodies at different temperatures is of fundamental importance in many nanotechnology applications. One such application is the nanoscale interface between the head and the disk in hard disk drives (HDDs). In order to read and write data, HDDs use a magnetic recording head with embedded read/write transducers that flies over a rotating magnetic disk (that stores the data). The disk's rotation pulls air into the interface between the head and the disk. Compression of the air in the head-disk interface (HDI) generates an air pressure driven lift force on the air bearing surface (ABS) of the slider. This air bearing lift allows the slider to fly over the disk at a distance known as the fly height (Fig. 1). To ensure a high storage density, contemporary Perpendicular Magnetic Recording (PMR) HDDs have a minimum fly height of less than 5 nm. Such a small controlled spacing is achieved via the Thermal-Fly Height Control (TFC) technology. A joule heater (see TFC heater in Fig. 1) is embedded near the slider's ABS close its trailing edge. The TFC heater is energized, causing a localized protrusion near the slider's trailing edge, thereby reducing the spacing between the head and the disk. The actuation of the TFC and the resultant fly height reduction has been extensively studied in literature[1–6]. Joule heating of the TFC heater in contemporary low-flying height PMR heads causes high temperatures in the head. Therefore, understanding head cooling via heat transfer in the HDI is a topic of utmost importance for HDD reliability.

Contemporary TFC sliders also have a resistive Embedded Contact Sensor (ECS) near the ABS (Fig. 1) that can be utilized to record the head surface temperature change due to heat transfer in the HDI and thereby indirectly detect head-disk contact[7]. The ECS has proved to be a useful aid in studying nanoscale heat transfer in the HDI in recent literature[8–13].

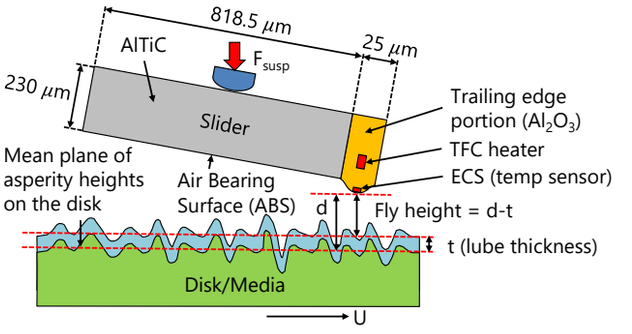


FIG. 1. Schematic of the Head-disk interface (HDI): We use the terms "disk" and "media" interchangeably in this study. The term "slider" refers to the entire block (843.5 $\mu m \times 700\ \mu m \times 230\ \mu m$). The slider block is composed of two parts - AlTiC (818.5 $\mu m \times 700\ \mu m \times 230\ \mu m$) and the trailing edge (TE) portion (25 $\mu m \times 700\ \mu m \times 230\ \mu m$) that is made of $Al_2O_3$. The term "head" typically refers to the local TE portion which contains the read/write transducers. The TFC heater is energized, causing a local protrusion near the trailing edge of the flying slider, thereby reducing the spacing between the head and the disk

Moreover, next-generation of HDD technologies like Microwave-Assisted Magnetic Recording (MAMR)[14] and Heat-Assisted Magnetic Recording (HAMR)[15] are currently being developed to supplant PMR and increase the storage density beyond 1 Tb/in$^2$. However, a major roadblock to the commercialization of both of these technologies is thermal reliability of the HDI due to high temperatures in the head.

a)Electronic mail: siddhesh_sakhalkar@berkeley.edu.

During HAMR writing, an optical system integrated into the head is used to locally heat the disk, generating high temperatures on the disk (∼500 $^{o}$C) and the head (∼300 $^{o}$C). These high temperatures further cause mass transfer in the HDI[16–18], leading to head contamination[19,20]. The Spin Torque Oscillator in MAMR heads experiences high current densities leading to similar overheating problems (temperature of >200$^{o}$ C)[21]. Understanding HDI nanoscale heat transfer is hence imperative to develop reliable head/media designs not only for PMR drives but also for HAMR and MAMR.

Traditionally, the heat transfer coefficient in the HDI is determined solely due to heat conduction through the pressurized air bearing by solving the energy equation using temperature jump theory[22,23]. However, when the fly height in contemporary HDDs becomes very low (< 5 nm), contributions due to near field radiation and phonon conduction also become significant[24–29]. Enhanced heat transfer at micro- and nano-scale gaps has been extensively studied in literature using experiments[30,31] and theoretical investigations[24–29,32–35]. It is imperative to consider radiation and phonon conduction heat transfer to accurately predict head temperatures in HDDs.

In our previous study[13], we performed static touchdown experiments[9] and simulations to study phonon conduction driven heat transfer between the head and the non-rotating media. We found that inclusion of phonon conduction, intermolecular forces and disk temperature rise is essential to accurately predict the ECS temperature during static touchdown. In this study, we aim to answer the next logical question: how much do phonon conduction, disk temperature rise and intermolecular forces impact the ECS temperature of a flying slider over a rotating disk?

While the effect of HDI intermolecular forces was considered in our previous static touchdown study[13], the roughness of the head and the disk was ignored. To consider the combined effect of intermolecular forces, head/disk roughness and head-disk contact, asperity based intermolecular adhesion force and contact force models are needed. Zheng & Bogy used the sub-boundary lubrication model proposed by Stanley et al.[36] to study the behaviour of a TFC slider flying at near-contact[37]. They found the fly height is significantly affected by adhesion and contact forces in the HDI. Moreover, the adhesion force also compromises the stability of the slider while flying at near-contact[37–39]. Since nanoscale heat transfer is spacing dependent, it is expected that adhesion and contact forces would impact the temperature profile of a flying slider.

Recently Zheng et al. numerically and experimentally studied the effect of the disk temperature rise on the ECS temperature for a flying slider over a rotating disk[11]. They found that the simulation that excludes the effect of disk temperature rise overestimates the ECS cooling. However, they did not study the ECS temperature change at contact conditions. Beyond contact, heat generation due to friction is expected to increase the ECS temperature[40,41].

In this paper, we introduce a numerical model to predict the temperature profile and the fly height for a TFC slider flying over a rotating disk. Next, we compare our simulations with touchdown experiments performed with a slider flying over a rotating Al-Mg disk. The TFC heater is energized, causing a localized protrusion near the slider's trailing edge and the ECS is utilized to record the temperature change (Fig. 1). The simulations and experiments are performed over a range of TFC powers starting from a fly height of ∼ 9-12 nm all the way down to contact. To accurately predict the fly height and heat transfer, we incorporate the effects of disk temperature rise, adhesion & contact force models, air & phonon conduction heat transfer and friction heating in our model. We study the effect of each of these features on the ECS temperature and the fly height during the flying touchdown process.

We first discuss the methodology used to compute the adhesion and contact forces and the net heat flux in the HDI in sections II A, II B and II C. Next, the overall simulation schematic, including the slider thermo-mechanical model, the disk thermal model and the air bearing model, is presented in sections II D, II E, II F and II G. This is followed by the results, discussion and conclusion in sections III, IV and V.

## II. MODEL DESCRIPTION

### A. ADHESION AND CONTACT FORCES

To accurately predict the fly height at near-contact, it is necessary to account for the interactions between the rough slider and the lubricant/rough disk using asperity-based intermolecular adhesion force and contact force models. In this study, we use the sub-boundary lubrication model which was proposed by Stanley et al.[36]. A rough surface (slider/disk) is described using three topological roughness parameters: standard deviation of asperity heights, mean radius of curvature of asperities and areal density of asperities. This model converts the problem of two contacting rough surfaces (slider and disk) to the equivalent simpler problem of contact between a rigid infinitely smooth surface (slider) and a nominally flat surface (disk) having combined roughness parameters of the individual surfaces. Accordingly, $\sigma_s$ is the standard deviation of asperity heights for the combined slider/disk surfaces, $R$ is the mean radius of curvature of asperities for the combined slider/disk surfaces and $\eta$ is the areal density of asperities for the combined slider/disk surfaces. We note that $\sigma_s$ is related to $\sigma$ (the standard deviation of surface heights for the combined slider/disk surfaces) as described in Ref. 36.

Next, the total intermolecular adhesion force $F_a$ between the slider and the lubricated disk is obtained as[36,37]

$$F_a = \eta A_n \left( \int_{-\infty}^{d-t} \frac{8}{3}\pi R\delta\gamma \left[ \left(\frac{\varepsilon}{d-u-t+\varepsilon}\right)^2 - \frac{1}{4}\left(\frac{\varepsilon}{d-u-t+\varepsilon}\right)^8 \right] \phi(u)\mathrm{d}u + 2\pi R\delta\gamma \int_{d-t}^{d} \phi(u)\mathrm{d}u + \int_{d}^{\infty}\int_{r_t}^{\infty} \frac{8}{3}\frac{\delta\gamma}{\varepsilon} \left[ \left(\frac{\varepsilon}{z-t+\varepsilon}\right)^3 - \left(\frac{\varepsilon}{z-t+\varepsilon}\right)^9 \right] 2\pi r\mathrm{d}r\phi(u)\mathrm{d}u \right) \tag{1}$$

where $A_n$ is the nominal contact area, $d$ is the distance between

TABLE I. Adhesion/contact force parameters[37,39,42–46]

| | |
|---|---|
| Combined standard deviation of surface heights $\sigma$ (nm) | 0.5 |
| Combined mean radius of asperities $R$ (nm) | 20 |
| Combined asperity density $\eta$ ($1/\mu m^2$) | 5000 |
| Equilibrium intermolecular distance $\varepsilon$ (nm) | 0.3 |
| Adhesion energy per unit area $\delta\gamma$ (N/m) | 0.1 |
| Lubricant thickness $t$ (nm) | 1 |
| Hertz elastic modulus $E$ (GPa) | 148.56 |

the mean plane of asperity heights on the disk and the slider ABS (Fig. 2), $t$ is the lubricant thickness, $\delta\gamma$ is the adhesion energy per unit area for the HDI, $\varepsilon$ is the equilibrium intermolecular separation, $u$ is the asperity height and $\phi(u)$ is the probability density function of asperity heights. We assume that $\phi(u)$ is a Gaussian distribution with a mean of zero and a standard deviation of $\sigma_s$. The expression for $z$ and $r_t$ (see Fig. 2) can be found in Refs. 36, 37. We note that since $d$ is the distance between the mean plane of asperity heights on the disk and the slider ABS, the fly-height (i.e. actual air bearing height) is defined as $h = (d - t)$ (as shown in Fig. 1). Eq. (1) considers three types of asperities on the disk (as shown in Fig. 2) - (1) non-contacting asperities (described by the first integral), (2) lubricant-contacting asperities (described by the second integral) and (3) solid-contacting asperities (described by the third integral).

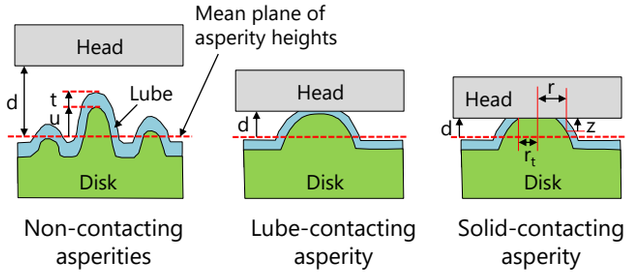


FIG. 2. The calculation of the adhesion force between the head and the disk using the sub-boundary lubrication model[36] (Eq. (1)) considers three types of disk asperities: non-contacting asperities, lubricant-contacting asperities and solid-contacting asperities

The contact force $F_c$ between the slider and the disk is obtained using the well-known Greenwood-Williamson model and is given by

$$F_c = \frac{4}{3}\eta A_n E R^{1/2} \int_d^\infty (u-d)^{3/2}\phi(u)\mathrm{d}u \tag{2}$$

where $E$ is the combined Hertz elastic modulus of the two surfaces. The adhesion and contact force parameters used in Eqs. (1), (2) are summarized in Table I.

## B. HDI HEAT TRANSFER COEFFICIENT

During flying touchdown of the slider on the disk, four major heat transfer schemes exist: air conduction ($htc_{air}$), viscous dissipation ($htc_{visc}$), phonon conduction ($htc_{phon}$) and radiation ($htc_{rad}$).

$$htc_{HDI} = htc_{air} + htc_{visc} + htc_{phon} + htc_{rad} \tag{3}$$

The heat transfer coefficient for conduction through air ($htc_{air}$) is a function of the air bearing height $h = (d - t)$, pressure $p_{air}$ and temperature $T_{air} = \frac{(T_s+T_d)}{2}$ and can be obtained by solving the energy equation using temperature jump theory[22,23].

$$htc_{air} = \frac{k_{air}}{h + 2\frac{2-\sigma_T}{\sigma_T}\frac{2\gamma}{\gamma+1}\frac{1}{Pr}\lambda_{air}} \tag{4}$$

Here $\lambda_{air}(h, p_{air}, T_{air})$ is the effective mean free path of air molecules at pressure $p_{air}$ and temperature $T_{air}$ accounting for boundary scattering[23] (with a nominal value of 67.1 nm for no boundary scattering and at ambient pressure and temperature). $k_{air}$ is the effective thermal conductivity of air accounting for boundary scattering (with a nominal value of 0.0261 W/(m-K) for no boundary scattering). $\sigma_T$ is the thermal accommodation coefficient, $Pr = 0.71$ is the Prandtl number of air and $\gamma = 1.4$ is the ratio of specific heats for air.

The thermal accommodation coefficient represents how a rarefied gas interacts with a solid surface, in terms of energy transfer between the colliding gas molecules and the surface. It is defined as follows: $\sigma_T = \frac{E_i - E_r}{E_i - E_w}$, where $E_i$ and $E_r$ are the energy of the incident and reflected molecules respectively and $E_w$ is the energy which would be carried away by the reflected molecules if the gas has had time to come to thermal equilibrium with the surface wall. The value of $\sigma_T$ depends on the gas and the surface properties such as the surface roughness, temperature, pressure, Knudsen number etc. and lies between 0 and 1. We assume that $\sigma_T = 0.6$ in our model[47,48]. This value ensures that the slope of the simulated ECS temperature change vs. TFC power curve in the initial linear regime agrees well with the corresponding experiment (see subsequent section III F). We note that since $\lambda_{air} \propto p^{-1}$, $htc_{air}$ increases as the air bearing pressure $p_{air}$ increases.

The heat transfer coefficient due to viscous dissipation ($htc_{visc}$) can be neglected compared to air conduction ($htc_{air}$) for small gap sizes[22] and hence is ignored in this study. The ratio of the magnitude of the viscous dissipation term to the magnitude of the air conduction term is about 0.01 for a slider-disk temperature difference of $\sim$20 °C[49].

We use a wave-based phonon conduction theory to model the enhanced nanoscale heat transfer due to van der Waals (vdW) force driven migration of phonons from one half-space to the other[25,27,28]. We consider a system of two half-spaces ($\nu = A, B$) separated by spacing $h$ and at distinct temperatures $T_A$ and $T_B$ (non-equilibrium condition). The net steady state phonon conduction heat flux between these two half-spaces is denoted by $Q$. We use the modified Planck function[29] to

describe the phonon waves in each half-space $\nu$.

$$(p_\nu^{\pm})^2(\omega,T_\nu,\mu_\nu)=\left(\exp\left(\frac{\hbar\omega[1\mp\mu_\nu]}{k_BT_\nu}\right)-1\right)^{-1} \quad (5)$$

Here $\omega$ is the wave frequency, $\mu_\nu$ is a factor that lies between 0 and 1 and represents how much the half-space $\nu$ has diverged from equilibrium, with $\mu_\nu=0$ as being at the equilibrium condition. $\hbar$ and $k_B$ are the reduced Planck constant, and the Boltzmann constant, respectively. In our notation, $p_\nu^+$ applies to waves travelling away from the half-space and $p_\nu^-$ applies to waves travelling into the half-space. As demonstrated in Refs. 27, 28, the heat flux $Q(T_A,T_B,h)$ can be described by

$$Q=N\int_\Omega\left\{(p_\nu^+)^2-(p_\nu^-)^2\right\}\frac{\hbar\omega^3}{8\pi^2c_\nu^2}\sin(2\theta_\nu)d\theta_\nu d\omega, \quad \nu=A,B, \quad (6)$$

where $N$ is the number of polarizations (= 3), $c_\nu$ is the wave speed, $\theta_\nu$ is the angle of propagation. The compatibility conditions from Ref. 28 establish the domain of integration $\Omega=\Omega(\omega,\theta_\nu)$ in Eq. (6) and are summarized below.

$$\Omega(\omega,\theta_\nu)=\begin{cases}F_-(\mu_A,T_A,\omega,\theta_A)\le f(\mu_B,T_B,\omega,\theta_B)\\ \le F_+(\mu_A,T_A,\omega,\theta_A),\\ F_-(-\mu_B,T_B,\omega,\theta_B)\le f(-\mu_A,T_A,\omega,\theta_A)\\ \le F_+(-\mu_B,T_B,\omega,\theta_B),\\ 0\le\omega\le\omega_D,\quad 0\le\theta_\nu\le\Theta_\nu.\end{cases} \quad (7)$$

Here $F_\pm$ and $f$ are

$$F_\pm(\mu_\nu,T_\nu,\omega,\theta_\nu)=|p_\nu^-(\omega,T_\nu,\mu_\nu)\pm Rp_\nu^+(\omega,T_\nu,\mu_\nu)|,$$
$$f(\mu_\nu,T_\nu,\omega,\theta_\nu)=\sqrt{1-R^2}p_\nu^-(\omega,T_\nu,\mu_\nu) \quad (8)$$
$$R\equiv R(\omega,\theta_\nu,h)$$

where $R$ is the reflection coefficient, $\omega_D$ is the Debye frequency of half-space $\nu$ and $\Theta_\nu$ is the critical angle for half-space $\nu$ (depends on $c_\nu$)[25,28]. The reflection coefficient $R$ influences $\Omega$ in Eq. (6) through Eqs. (7), (8), thereby regulating how much heat flows from one half-space to the other because of vdW forces. We note that $R(\omega,\theta_\nu,h)$ also depends on the material density $\rho_\nu$ and the acoustic wave speed $c_\nu$[25].

We have 3 unknowns in this problem $(Q,\mu_A,\mu_B)$, but only 2 equations from (6). A unique solution is obtained by maximizing $Q$ in order to maximize the entropy of the system[28,50]. Accordingly, we compute the phonon conduction heat transfer coefficient for the HDI ($htc_{phon}=\frac{Q(\hat{T}_s,\hat{T}_d,h)}{\hat{T}_s-\hat{T}_d}$) as a function of $h$, $\hat{T}_d$ and $\Delta\hat{T}=\hat{T}_s-\hat{T}_d$. Here $\hat{T}_d$ and $\hat{T}_s$ are the disk and slider surface temperatures respectively. The results for the computed $htc_{phon}$ for the HDI are described in subsequent section III A.

We ignore radiative heat transport in this study, since $htc_{rad}$ ($\sim10^3$ W/m$^2$·K)[26] is typically much smaller than $htc_{phon}$ ($\sim10^6$ W/m$^2$·K) at nanoscale spacings. Thus, the net heat transfer coefficient in the HDI is approximated as:

$$htc_{HDI}\approx htc_{air}+htc_{phon} \quad (9)$$

### C. FRICTION HEATING FLUX

The net heat generation per unit contact area due to friction heating is given by[40]

$$q_{fric}=\mu pU \quad (10)$$

Here $\mu$ is the coefficient of friction, $p$ is the net normal pressure in the HDI due to the contact force and the adhesion force[51] and $U$ is the linear disk speed. We assume a heat partition factor of 0.5 in our model[40] so that the heat flux due to friction heating into the slider ($q_{fric,s}$) and the disk ($q_{fric,d}$) is given by $q_{fric,s}=q_{fric,d}=0.5q_{fric}$.

### D. SLIDER THERMO-MECHANICAL MODEL

We determine the slider temperature profile $T_s(x,y,z)$ and thermal protrusion due to TFC heating using a thermo-mechanical finite element model (ANSYS). The net heat flux into the slider ABS due to heat transfer in the HDI and heat generation due to friction is given by

$$q_s=-htc_{HDI}(\hat{T}_s-\hat{T}_d)+q_{fric,s} \quad (11)$$

We note that $T_s(x,y,z)$ and $T_d(x,y,z)$ are the temperature profiles in the slider and the disk respectively. On the other hand, $\hat{T}_s(x,y)=T_s(x,y,z=0)$ is the slider ABS surface temperature and $\hat{T}_d(x,y)=T_d(x,y,z=0)$ is the disk top surface temperature profile (as shown in Fig. 3).

As shown in Fig. 1, the slider is composed of two parts - a block of 818.5 $\mu m\times700\ \mu m\times230\ \mu m$ that is made of AlTiC (thermal conducitivity of 20 W/m·K)[1] and a block of 25 $\mu m\times700\ \mu m\times230\ \mu m$ (called the trailing edge or TE portion) that is made of $Al_2O_3$ (thermal conductivity of 1.8 W/m·K)[1]. We use a similar model as Ref. 13 to account for the presence of the metallic components in the TE body (such as the NiFe reader, Cu writer and NiFe shields), which have a much higher thermal conductivity (35 W/m·K for NiFe, 403 W/m·K for Cu)[1] than $Al_2O_3$. These metallic components are present near the ABS in a volume of 25 $\mu m\times30\ \mu m\times35\ \mu m$ and are described in our model using an effective thermal conductivity of 50 W/m·K and an effective thermal expansion coefficient of 8e-6 K$^{-1}$ as described in Ref. 13. Using a similar slider model, we obtained a good agreement between simulations and experiments for static touchdown of the head on different media materials (AlMg disk, glass disk and Si wafer), in different environments (air, vacuum) and at different head-media spacings in our previous study[13]. The slider model is meshed using quadratic tetrahedral elements ($\sim$ 65000 elements). The mesh of the slider is refined at the TFC protrusion area near the trailing edge to accurately simulate the temperature distribution and the deformation in this region and ensure grid independence of the solution.

We perform a static thermal finite element analysis to compute the slider temperature profile ($T_s$) due to TFC joule heating. We consider a convection coefficient of 100 W/m$^2$·K on the side surfaces and a larger convection coefficient of 2000 W/m$^2$·K) on the back surface of the slider to account for metal fixture cooling[52]. The ambient temperature and pressure are

set as 25°C and 101325 Pa for the simulation. The heat flux $q_s$ from Eq. (11) is applied on the ABS. The temperature profile generated by the thermal analysis ($T_s$) is subsequently used to determine the thermal protrusion of the slider using a static structural finite element analysis. The air bearing pressure profile, adhesion force and contact force are applied on the slider ABS in this structural simulation. The two corners at the leading edge on the back of the slider are fixed. The back of the slider is constrained in the height ($z$) direction.

## E. DISK THERMAL MODEL

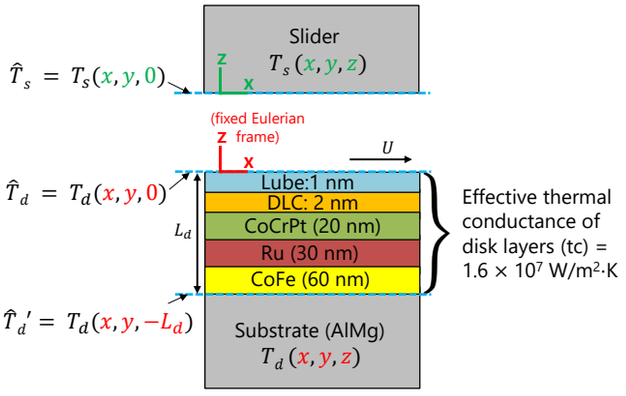


FIG. 3. PMR slider and disk schematic. PMR disks have a multi-layered structure comprising of the lubricant, diamond-like-carbon (DLC), the magnetic layers (CoCrt, Ru, CoFe) and the AlMg substrate.

As the disk rotates underneath the flying hot slider, heat transfers from the slider to the part of the disk which is underneath the slider at any given time. Hence, the temperature of each material point on the disk varies periodically and does not reach a steady state.

We note that the slider's dimension is significantly smaller than the disk's circumference (by a factor < 0.01). Secondly, the disk has uniform material properties throughout the x-y plane. We now change our viewpoint from the disk to the slider, i.e., we fix the coordinates with the stationary slider and use a Eulerian description of the disk temperature field, $T_d(x,y,z)$. The advantage of using Eulerian co-ordinates is that the temperature field in this coordinate system does reach a steady state (i.e. does not change with time). This same technique has been used in heat transfer textbooks[53,54] to study the problem of a stationary heat source acting on the surface of a moving semi-infinite medium problem. We also note that a similar methodology was used in Ref. 11 to determine the temperature rise of the rotating disk due to heat transfer from the slider. Accordingly, the heat equation for $T_d$ needs to be reformulated using Eulerian coordinates. Ignoring the skew of the slider, the temperature profile of the disk in this co-ordinate system is given by

$$\rho C_p U \frac{\partial T_d}{\partial x} = \nabla.(k \nabla T_d) \tag{12}$$

Here $\rho$ is the density, $C_p$ is the specific heat capacity, $U$ is the linear disk speed and $k$ is the thermal conductivity. The net heat flux into the disk due to heat transfer from the slider and heat generation due to friction heating is obtained as

$$q_d = htc_{HDI}(\hat{T}_s - \hat{T}_d) + q_{fric,d} \tag{13}$$

Eq. (12) subject to boundary condition Eq. (13) determines the disk temperature profile.

We describe the thin layers (lubricant, Diamond-like-Carbon, magnetic layers) on the top of the AlMg substrate of the PMR disk (Fig. 3) using an "effective thermal conductance" ($tc = 1.6 \times 10^7$ W/m$^2$·K) in our model[13]. This approximation assumes that the temperature varies linearly along each layer thickness (i.e. heat flux along the $z$ direction remains a constant through the layers). Accordingly, we compute the temperature jump between the top surface of the PMR disk ($\hat{T}_d$) and the top surface of the AlMg substrate ($\hat{T}_d' = T_d(x,y,z=-L_d)$) as (see Fig. 3)

$$q_d = tc(\hat{T}_d - \hat{T}_d') \tag{14}$$

Assuming that the AlMg disk substrate can be approximated as a semi-infinite medium, the temperature profile of the top surface of the AlMg substrate ($\hat{T}_d'$) is determined using the analytical solution of Eq. (12) as[54].

$$\hat{T}_d'(x,y) = T_0 + \int\int \frac{q_d(x',y')}{2\pi k R} e^{-\frac{U\rho C_p}{2k}(R-(x-x'))} dx'dy'$$
$$R = \sqrt{(x-x')^2 + (y-y')^2} \tag{15}$$

Here $T_0 = 298$ K is the ambient temperature. $\rho$, $C_p$, $k$ for AlMg can be found in Ref. 55. Eqs. (13), (14) and (15) together describe the temperature profile of the top surface of the disk $\hat{T}_d$.

## F. AIR BEARING PRESSURE SOLVER

We use a modified version of the CML Air static simulation program[56] to solve for the air bearing pressure distribution and the steady-state fly height. CML Air determines an equilibrium flying state (fly height, pitch, roll) of a slider for a given suspension load using a Quasi-Newton method. The air bearing pressure is computed by solving the generalized Reynolds equation with the Fukui–Kaneko slip correction. CML Air uses Patankar's control volume method with a multigrid solver to discretize and solve the generalized Reynolds equation[56].

The sub-boundary lubrication model[36] is implemented in the modified CML Air program by regarding the slider ABS as an infinitely smooth surface with combined roughness parameters being applied on the disk surface (see Table I)[37,57]. The asperity heights on the disk are described by a Gaussian distribution function $\phi(u)$ with a mean of zero and a standard deviation $\sigma_s$. This asperity-based model enables us to solve the generalized Reynolds equation at near-contact and contact conditions when the fly height $(d-t)$ becomes 0 or even negative[38,57]. This approach also considers the effect of air pressure loss at asperities which are in contact during determination of the air bearing force and the air conduction heat

flux[38,57]. The ABS profile is modified with the simulated TFC protrusion[57] using the slider thermo-mechanical finite element model (section II D) to account for the fly height change due to TFC actuation. The equilibrium flying state of the slider is then determined by balancing the forces and torques on the slider due to adhesion and contact forces (Eqs. (1), (2)), the suspension load and the air bearing pressure[37,57].

### G. OVERALL SIMULATION METHODOLOGY

The simulated TFC protrusion profile determined by the slider thermo-mechanical model is used to compute the steady state fly-height and air bearing pressure using the modified CML Air program (accounting for adhesion and contact forces in the HDI using Eqs. (1), (2)). The fly height, air pressure $p_{air}$, slider surface temperature $\hat{T}_s$ and disk surface temperature $\hat{T}_d$ are used to compute the heat flux into the slider and disk $q_s$, $q_d$ using Eqs. (9), (10), (11), (13). $q_s$ and $q_d$ are further used as boundary conditions to determine the slider temperature profile $T_s(x,y,z)$ and the disk temperature profile $T_d(x,y,z)$ as described in sections II D and II E. $T_s$, $p_{air}$ and the computed adhesion and contact forces on the ABS in the modified CML Air are used to determine the slider TFC heating-induced protrusion profile as described in section II D. The resultant non-linear problem involving the modified CML Air, the slider thermo-mechanical model and the disk thermal model is solved using Broyden's Quasi-Newton method. The overall simulation schematic is summarized in Fig. 4.

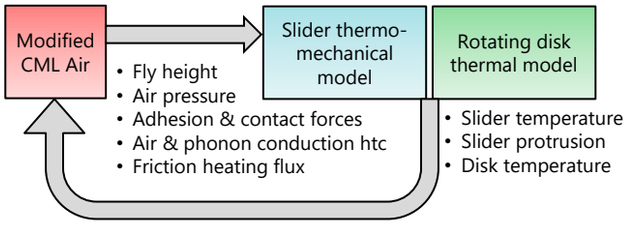


FIG. 4. Overall simulation model schematic: Modified CML Air is used to compute the slider's fly height, the air pressure distribution, the adhesion & contact forces and the net heat flux due to air & phonon conduction and friction heating. The slider thermo-mechanical model and the disk thermal model are used to compute the slider and disk temperature profiles and the slider's protrusion. The resultant non-linear problem is solved using Broyden's method

## III. RESULTS AND DISCUSSION

### A. PHONON CONDUCTION HEAT TRANSFER COEFFICIENT

In our previous study[13], we determined $htc_{phon}$ as a function of $h$, $\hat{T}_d$ and $\Delta\hat{T} = \hat{T}_s - \hat{T}_d$ for the HDI, assuming that the slider material is $Al_2O_3$ and the disk material is AlMg/glass.

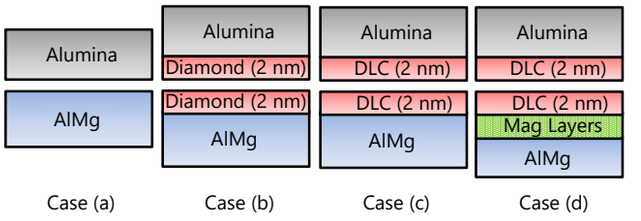


FIG. 5. Phonon conduction calculation cases for Fig. 6

We found that $htc_{phon}$ can be well approximated with the following equation (0.1 nm $\leq h \leq$ 100 nm, 4 K $\leq \Delta\hat{T} \leq$ 400 K, 298 K $\leq \hat{T}_d \leq$ 398 K)[13]

$$ln(htc_{phon}) = c_1 ln(h) + c_2 ln\left(\frac{\Delta\hat{T}}{400}\right) + c_3 ln\left(\frac{\hat{T}_d}{298}\right) + b \quad (16)$$

Parameters $c_1$, $c_2$, $c_3$, $b$ depend on the material properties of both half-spaces ($\rho_v$, $c_v$ and $\omega_D$) .

However, we did not consider the effect of the diamond-like-carbon (DLC) films on the slider/disk and the magnetic layers on the disk (Fig. 3) in our previous study[13]. Other studies have shown that addition of a diamond film to the disk can significantly reduce the phonon conduction heat transfer coefficient[25]. To understand the effect of slider/disk DLC films and disk magnetic layers on phonon conduction, we consider 4 cases as shown in Fig. 5:

(a) $Al_2O_3$ - gap - AlMg

(b) $Al_2O_3$ - 2 nm Diamond layer - gap - 2 nm Diamond layer - AlMg

(c) $Al_2O_3$ - 2 nm DLC layer - gap - 2 nm DLC layer - AlMg

(d) $Al_2O_3$ - 2 nm DLC layer - gap - 2 nm DLC layer - mag layers - AlMg

The material properties ($\rho_v$, $c_v$, $\omega_D$) of all the layers are summarized in Table II. We use bulk Diamond properties for the Diamond layer (case b) and thin film DLC properties for the DLC layer (cases c and d). The thin film DLC acoustic wave speed is estimated from the elastic properties and density of a 2.2 nm DLC film from Ref. 58. The acoustic wave speed of the magnetic layer materials is estimated from the elastic properties and density from Ref. 55.

The resultant $htc_{phon}$ as a function of $h$ for cases (a), (b), (c), (d) are plotted in Fig. 6. Our results show that the addition of a 2 nm Diamond layer (with bulk Diamond properties) reduces the phonon conduction heat transfer coefficinet by 1 to 2 orders of magnitude (which is consistent with previously published results in Ref. 25). However, addition of a 2 nm DLC layer (with thin film DLC properties) has a relatively small effect on $htc_{phon}$. Similarly, addition of a 2 nm DLC layer and magnetic layers also has a relatively small effect on $htc_{phon}$.

The acoustic wave speed of Diamond is much larger than that of AlMg and Alumina, hence the acoustic impedance

TABLE II. Density, acoustic wave speed and Debye frequency of different materials for computation of $htc_{phon}$[55,58,59]

| Material | $\rho_v$ (kg/m$^3$) | $c_v$ (m/s) | $\omega_D$ ($\times 10^{15}$ rad/s) |
|---|---|---|---|
| Alumina | 3980 | 7133 | 0.1179 |
| AlMg | 2660 | 3420 | 0.056 |
| Diamond | 3500 | 13850 | 0.2919 |
| DLC | 2800 | 4167 | 0.1593 |
| CoCrPt | 8900 | 2844 | 0.06 |
| Ru | 12300 | 2295 | 0.0726 |
| CoFe | 8514 | 2601 | 0.06 |

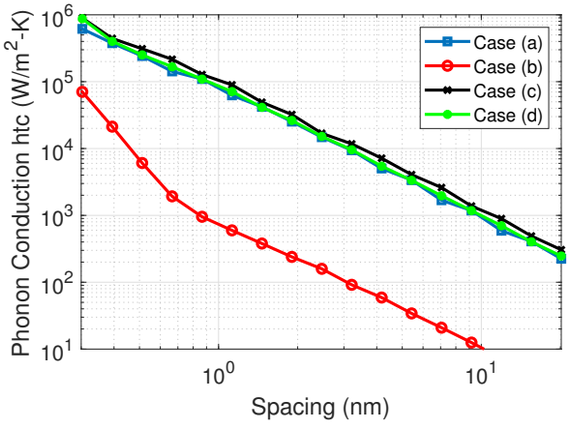


FIG. 6. Phonon conduction heat transfer coefficient as a function of spacing $h$ for cases (a), (b), (c), (d). These plots are for $\Delta\hat{T} = \hat{T}_s - \hat{T}_d = 400$ K and $\hat{T}_d = 298$ K. Here $\hat{T}_d$ and $\hat{T}_s$ are the disk and slider surface temperatures respectively.

(defined as the product of the density and the acoustic wave speed) of Diamond is also larger than that of AlMg and Alumina. A large impedance mismatch between the materials leads to a high reflection coefficient (closer to 1) and high scattering of acoustic waves across their interface, which in turn reduces the phonon conduction heat transfer coefficient[25]. Accordingly, the large impedance mismatch between the Diamond layer and the half space materials (AlMg and Alumina) causes the simulation case (b) to show a significantly smaller $htc_{phon}$ than the simulation case (a). On the other hand, the impedance of the DLC layer and the magnetic layers lies in between the impedance for AlMg and the impedance for Alumina. Hence, we have a smaller impedance mismatch between the layer materials and the half-space materials (AlMg and Alumina) for cases (c), (d). Hence, the cases (c), (d) show a similar $htc_{phon}$ compared to case (a). Nevertheless, we use the simulation curve for case (d) for all the simulations in this study. For case (d), the parameters in Eq. (16) are obtained as: $c_1 = -1.99$, $c_2 = -0.83$, $c_3 = 0.99$, $b = 11.4$.

## B. EFFECT OF DISK TEMPERATURE RISE

In this section, we study the effect of the disk temperature rise on the ECS temperature. Fig. 7 plots the ECS temperature change vs. the TFC power for the simulations with and without the disk temperature model. In the simulation with the disk temperature model, the disk temperature rise is determined using the methodology described in Section II E. In the simulation without the disk temperature model, the disk is assumed to be an ideal heat sink and hence the disk temperature is always equal to the ambient temperature everywhere (i.e. $T_d(x,y,z) = T_0 = 298$K). Both simulations include heat transfer due to both air and phonon conduction. For now, adhesion and contact forces and friction heating are excluded in both simulations.

In both simulations, initially, the ECS temperature increases with increasing TFC power due to larger joule heating generated at the higher TFC power. However, as the flying head approaches the rotating disk with a further increase in TFC power, enhanced nanoscale heat transfer in the HDI due to air conduction and phonon conduction causes the ECS temperature to decrease. Our results indicate that the simulation without the disk temperature model overestimates the ECS cooling drop compared to the simulation with the disk temperature model. The simulation with the disk temperature model shows a small ECS cooling drop of 1.7 $^o$C, while the simulation without the disk temperature model shows a large drop of $>8^o$C. We note that a similar trend was observed in Ref. 11. The heat flux from the slider to the disk is directly proportional to the temperature difference between the slider and the disk surfaces (Eq. (11)). Treating the disk as an ideal heat sink overestimates the heat flux in the HDI and hence overestimates the ECS cooling drop.

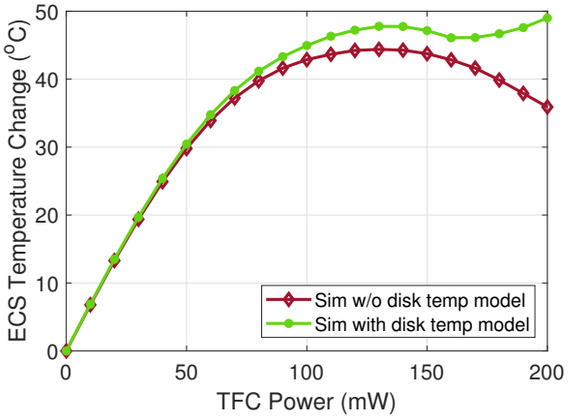


FIG. 7. ECS temperature change vs. the TFC power for the simulations with and without the disk temperature model. The simulation with the disk temperature model shows a smaller ECS cooling drop compared to the simulation without the disk temperature model.

### C. EFFECT OF ADHESION AND CONTACT FORCES

The adhesion and contact forces in the HDI are computed as a function of the fly height using eqs. (1), (2) and are plotted in Fig. 8. We note that adhesion force being attractive is negative and the contact force being repulsive is positive. We also note that $d$ is the distance between the mean plane of asperity heights on the disk and the slider ABS and the fly height is defined as $(d-t)$, hence the fly height becomes negative when the head protrusion penetrates into the lubricant. We see that as the fly height becomes smaller than $\sim$ 1 nm, the magnitude of the adhesion force starts increasing due to enhanced head-lubricant-disk interactions, causing the net normal force to decrease. As the fly height is further decreased causing the head to penetrate through the lubricant and come into contact with the disk asperities, the contact force increases rapidly, causing the net normal force to increase.

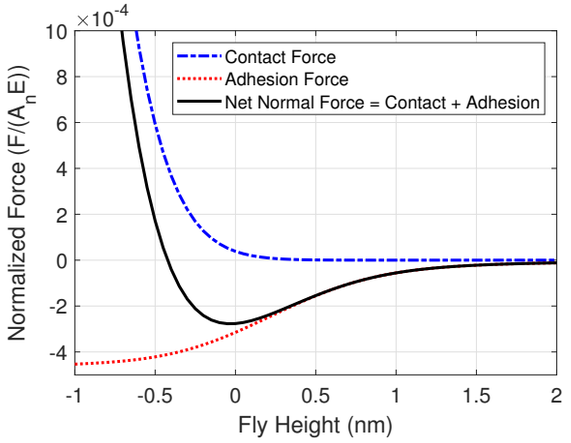


FIG. 8. Adhesion and contact forces in the HDI as a function of the fly-height $(d-t)$. Here $d$ is the distance between the mean plane of asperity heights on the disk and the slider ABS and $t$ is the lubricant thickness. Hence the fly height becomes negative when the head protrusion penetrates into the lubricant.

In order to study the effect of adhesion/contact forces on fly height and nanoscale heat transfer, we perform simulations with and without adhesion/contact forces. We plot the minimum fly height vs. the TFC power for the simulations with and without adhesion/contact forces in Fig. 9 (left axis). Both simulations include the disk temperature rise model and heat transfer due to both air and phonon conduction. Friction heating is excluded in both simulations.

The simulation with adhesion/contact forces has a lower fly height (8.94 nm) than the simulation without adhesion/contact forces (10.16 nm) at TFC power = 0 mW. This is because attractive adhesion forces between the head and the disk cause the head to fly at a lower spacing. As the TFC power is increased and the minimum fly height decreases below $\sim$ 1.2 nm (TFC power $>$ 77.5 mW), the magnitude of the adhesion force starts increasing (Fig. 8), causing the simulation with adhesion/contact forces to reach touchdown at a lower TFC power than the simulation without adhesion/contact forces (Fig. 9).

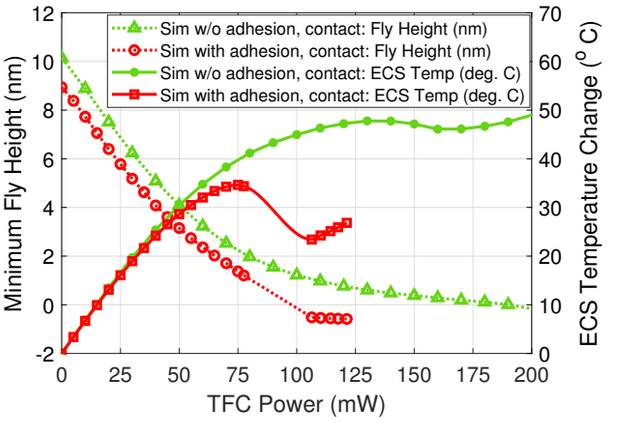


FIG. 9. Comparison between simulations with and without adhesion & contact forces: minimum fly height (left axis) and ECS temperature change (right axis) vs. TFC power. Attractive adhesion between the head and the disk causes a reduction in fly height and a steeper ECS cooling drop for the simulation with adhesion/contact forces as compared to the simulation without adhesion/contact forces.

Moreover, since the adhesion force acts in a direction opposite to the air bearing force, the slider looses stability when the increase in the air bearing force can no longer balance the rapid increment in adhesion force[37]. Hence, we do not find stable equilibrium fly heights between 77.5 mW and 106.4 mW. The slider regains stability when it comes into contact with the disk at TFC power of 106.4 mW (minimum fly height = - 0.52 nm). The rapidly growing contact force adds on to the air bearing force (Fig. 8) thereby restoring the stability of the HDI[37]. We use the approach discussed in Refs. 37, 60 to determine the stability of an equilibrium state.

The instability in the fly height of TFC sliders at near-contact has been observed in several previous simulation studies[37–39,44]. This instability has also been observed experimentally in literature using an LDV to measure slider vertical vibration and AE signal to monitor contact at the HDI[61–63]. To model the slider behavior during this unstable region, simulations need to be performed with a dynamic air bearing program (such as the CML Air dynamic simulation program) so as to capture the bouncing vibrations of the slider[38,39].

The loss of slider stability with rapidly increasing adhesion forces beyond 77.5 mW makes the convergence of the simulation scheme (Fig. 4) challenging. Hence, to simplify the highly non-linear calculations at near-contact, we use the methodology from Ref. 37 - we set the slider protrusion profile at TFC power of 70 mW as a baseline and proportionally alter this profile for TFC power beyond 77.5 mW for the simulation with adhesion/contact forces.

We also plot the ECS temperature change vs. the TFC power for the simulations with and without adhesion/contact forces in Fig. 9 (right axis). As the head-disk spacing decreases, the heat transfer coefficient due to air conduction as well as phonon conduction increases (Eq. (4), Fig. 6). Hence, as the head approaches the disk with increasing TFC power,

enhanced heat transfer in the HDI due to both air conduction and phonon conduction leads to a drop in the ECS temperature change vs. TFC power curve. The simulation with adhesion/contact forces has a smaller spacing and hence a larger heat transfer coefficient than the simulation without adhesion/contact forces (Fig. 9). Hence, the simulation with adhesion/contact forces shows a smaller ECS temperature and a steeper ECS cooling drop than the simulation without these forces.

We note that we observed a similar trend (compared to Fig. 9) in our previous static touchdown simulation study[13], where the simulation with intermolecular forces showed a steeper ECS cooling drop than the simulation without intermolecular forces.

### D. EFFECT OF PHONON CONDUCTION AND FRICTION HEATING

The net heat flux in the HDI has three dominant contributions: air conduction, phonon conduction and friction heating (Eqs. (9), (11), (13)). To isolate these effects, we performed simulations for the following four cases:

(a) Simulation without $htc_{phon}$ and without friction heating

(b) Simulation with $htc_{phon}$ and without friction heating

(c) Simulation without $htc_{phon}$ and with friction heating

(d) Simulation with $htc_{phon}$ and with friction heating

We plot the the ECS temperature change vs. TFC power curve for all four cases in Fig. 10. All four simulation cases consider air conduction heat transfer $htc_{air}$, the disk temperature rise model and adhesion/contact forces. We assume that the friction coefficient $\mu = 0.7$ for the cases (c) and (d) in Fig. 10.

To isolate the effects of air conduction and phonon conduction, we compare the cases (a) and (b) in Fig. 10. For TFC power $<$ 77.5 mW (i.e. fly height $>$ 1.2 nm), simulations with and without phonon conduction give very similar results, indicating that air conduction is the dominant heat transfer mechanism for large fly heights. However, when the fly height becomes smaller than 1.2 nm (TFC Power $>$ 77.5 mW), the simulation with phonon conduction (case (b)) shows a larger ECS cooling drop than the simulation without phonon conduction (case (a)). We observe an ECS cooling drop of 11.2 $^{o}$C for case (b) vs 7.8 $^{o}$C for case (a). Our results indicate that it is imperative to include phonon conduction heat transfer to accurately predict the ECS temperature at near-contact.

Comparing cases (c) and (d) in Fig. 10, we note that the addition of phonon conduction causes a larger ECS cooling drop (i.e. phonon conduction is a major contributor to the total heat flux in the HDI) even when friction heating is included.

Next, we study the effect of friction heating on the ECS temperature change vs. TFC power curve by comparing cases (b) and (d) in Fig. 10. As expected, both simulations yield exactly identical results at large fly heights (TFC power $\leq$ 77.5 mW). Further, as noted in section III C, we do not find stable equilibrium fly heights and ECS temperatures between 77.5 mW and 106.4 mW for the simulation without friction heating (case (b)) and between 77.5 mW and 102 mW for the simulation with friction heating (case (d)) due to the inclusion of adhesion and contact forces. Beyond contact, the simulation with friction heating shows a larger ECS temperature change and a larger slope of ECS temperature change vs. TFC power due to additional heat generated by friction.

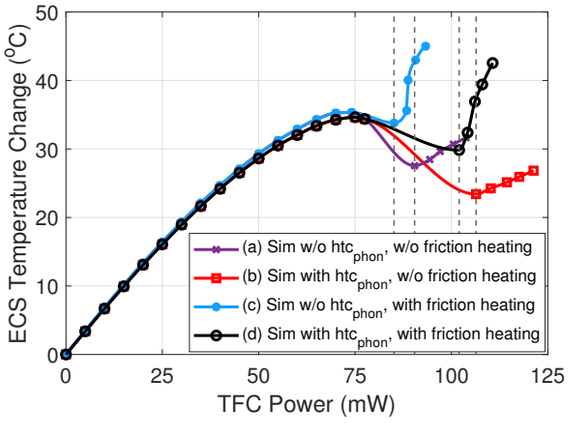


FIG. 10. Comparison between simulations with and without phonon conduction (case (a) vs. case (b)) and simulations with and without friction heating (case (b) vs. case (d)). The simulation with phonon conduction (case (b)) shows a larger ECS cooling drop than the simulation without phonon conduction (case (a)). The simulation with friction heating (case (d)) shows a larger ECS temperature slope beyond contact than the simulation without friction heating (case (b)). The vertical lines indicate the TFC power at which contact occurs.

### E. EFFECT OF INTERFACE THERMAL CONDUCTANCE

We plot the temperature change at the ECS (which is located near the head ABS, see Fig. 1) and the temperature change at the location on the surface of the disk exactly below the ECS at different TFC powers in Fig. 11. We note that this simulation considers the effects of disk temperature rise model, heat transfer due to both air and phonon conduction, adhesion/contact forces and friction heating.

As the spacing $h$ decreases, the net heat transfer coefficient in the HDI due to phonon and air conduction, $htc_{HDI}$ increases (Eq. (4), Fig. 6). Hence, as the TFC power is increased (causing $h$ to decrease), the head and the disk temperatures at the ECS location approach each other, as shown in Fig. 11. In reality, at head-disk contact, $htc_{HDI}$ would be restricted by the interface thermal conductance of the HDI. Hence, we enforce an interface thermal conductance of $1.5 \times 10^{7}$ W/m$^{2}$·K as an upper bound to $htc_{HDI}$ in our model (case (a) in Fig. 11). We note that this same value of the interface thermal conductance has also been used in all the rest of the simulations performed in this study.

While the interface thermal conductance of phonon mediated interfaces typically lies in the range $8 \times 10^{6}$ to $7 \times 10^{8}$

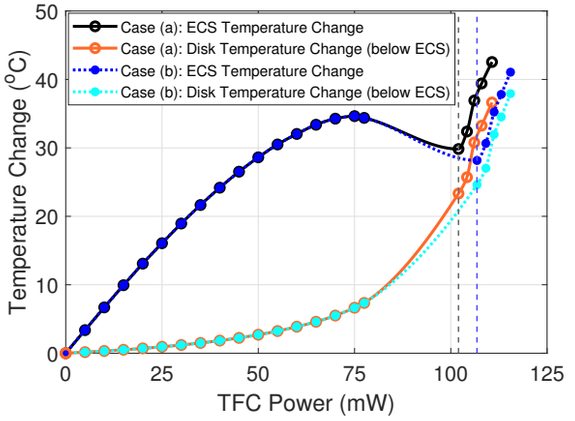


FIG. 11. Comparison between the temperature change at the ECS (on the head surface) and the temperature change at the location on the disk exactly below the ECS for different TFC powers. The interface thermal conductance is assumed to be $1.5 \times 10^7$ W/m$^2$·K for case (a) and $3 \times 10^7$ W/m$^2$·K for case (b). The vertical lines indicate the TFC power at which contact occurs (102 mW for case (a) and 106.8 mW for case (b)).

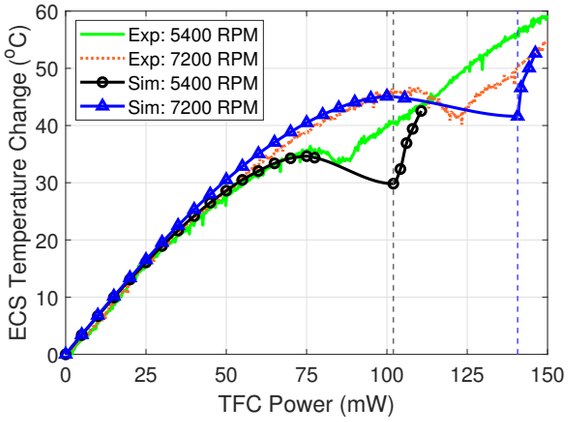


FIG. 12. Comparison between simulation and experiment at 5400 RPM & 7200 RPM: ECS temperature change vs. TFC power. The vertical lines indicate the TFC power at which contact occurs (102 mW for 5400 RPM and 140.7 mW for 7200 RPM).

W/m$^2$·K[64,65], its precise value for the HDI is unclear and is also expected to depend on the surface roughness of the disk/head[65]. In order to study the impact of the assumed value of the interface thermal conductance, we also perform a simulation with a higher interface thermal conductance of $3 \times 10^7$ W/m$^2$·K (case (b) in Fig. 11). Due to the presence of this interface thermal conductance, the head and disk temperatures are not exactly equal even at and beyond touchdown (i.e. TFC power $\geq$ 102 mW for case (a) and TFC power $\geq$ 106.8 mW for case (b)). Rather we see a temperature jump of $\sim 6$ ° C for case (a) and $\sim 3$ ° C for case (b) between the head and the disk at the ECS location beyond contact. A higher interface thermal conductance results in a smaller temperature jump between the slider and the disk at contact.

### F. COMPARISON WITH EXPERIMENTS

Fig. 12 shows the simulated ECS temperature change vs. TFC power curve at 5400 RPM and 7200 RPM and comparison with corresponding experimental curves. The minimum fly height vs. TFC power for the simulations at 5400 RPM and 7200 RPM are plotted in Fig. 13. Both the simulation and the experiment are performed at a radial position of 27 mm. Both simulations consider the disk temperature rise model, heat transfer due to both air and phonon conduction, adhesion/contact forces and friction heating. The simulation at 5400 RPM is performed with $\mu = 0.7$ and the simulation at 7200 RPM assumes $\mu = 0.5$. The smaller $\mu$ at 7200 RPM can be justified by the larger sliding velocity and the larger normal force at 7200 RPM compared to 5400 RPM. All other parameters are kept the same for both simulations (5400 RPM and 7200 RPM).

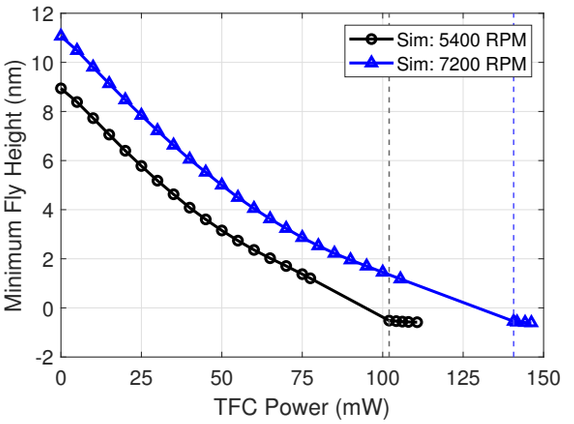


FIG. 13. Comparison between simulations at 5400 RPM and 7200 RPM: minimum fly-height $(d-t)$ vs. TFC power. The simulation at 7200 RPM has a larger fly height (at a given TFC power) and a larger touchdown power (140.7 mW) than the simulation at 5400 RPM (102 mW). The vertical lines indicate the TFC power at which contact occurs.

As expected, the simulation at 7200 RPM has a larger fly height (at a given TFC power) and a larger touchdown power than the simulation at 5400 RPM. As explained in section III C, we do not find stable equilibrium fly heights and ECS temperatures between 77.5 mW and 102 mW for the simulation at 5400 RPM due to the inclusion of adhesion and contact forces. The simulation at 7200 RPM also shows a similar behavior with no stable equilibrium fly heights and ECS temperatures between 105.5 mW and 140.7 mW.

The value of the thermal accommodation coefficient $\sigma_T = 0.6$ in Eq. (4) is chosen such that the slope of the ECS temperature vs. TFC power curve in the initial linear regime in

the simulation ($\sim$0.63 $^{o}$C/mW from 0 to 30 mW) agrees well with the corresponding initial slope in the experiment at 5400 RPM. With $\sigma_T = 0.6$, we see that overall the simulated ECS temperature change vs. TFC power curves at both 5400 RPM and 7200 RPM agree reasonably well with corresponding experimental curves even beyond the initial linear regime of 0 to 30 mW.

However, we note that the rate of frictional heating in the simulation is higher than the experimental observation (i.e. slope of ECS temperature change vs. TFC power beyond contact is higher in the simulation than the experiment). This may be caused by several factors such as:

- We assume a constant friction coefficient $\mu$ at a given sliding velocity in our simulations. In reality, $\mu$ is a function of the normal pressure (typically $\mu$ decreases with increasing normal pressure). Hence as the TFC power is increased beyond the touchdown power and the contact pressure increases, assuming a constant $\mu$ at the higher contact pressure may cause the simulation to overestimate the amount of friction heating.
- The contact force estimated by the simulation (Eq. (2)) may be higher than reality, causing the simulation to overestimate friction heating
- The TFC protrusion shape predicted by the simulation at contact and hence the simulation contact area may be different than reality

## IV. DISCUSSION

Understanding head cooling via nanoscale heat transfer in the HDI is important for thermal management of HDDs. In contemporary PMR drives, TFC/writer coil joule heating and frictional heating can lead to high temperatures in the head. One way to address this issue is to modify the ABS design so as to alter the air bearing pressure distribution and the flying attitude of the slider, thereby changing the HDI heat transfer coefficient. The slider trailing edge design (such as the reader, writer, shields) can also influence heat diffusion in the head. Our results indicate that it is imperative to account for the disk temperature rise, adhesion and contact forces, both air and phonon conduction and friction heating to accurately predict the head cooling due to HDI heat transfer. These features should be incorporated in any simulation model that is used to compare different ABS designs or different head designs in the context of their thermal performance. The problem of head overheating is more pronounced in the case of HAMR and MAMR. While this study uses PMR heads and disks, the methodology developed here can also be extended to predict the head temperature for flying HAMR and MAMR heads. Our hope is that our findings would provide a better understanding of the mechanism of heat transfer in the HDI and would contribute towards managing head overheating in PMR, HAMR and MAMR drives.

The simulation model presented in this study can be improved by modeling the detailed head geometry including the reader, writer and shields. While intermolecular van der Waals forces are the driving mechanism for phonon conduction heat transfer between two half-spaces, the high air bearing pressure in the HDI may also enhance the $htc_{phon}$. Humidity in the HDI can also affect the air pressure, fly height and air conduction/phonon conduction heat transfer coefficients, which is not considered in our study[66]. The accuracy of the simulated ECS temperature and fly height at near-contact can be improved by considering the thermal protrusion of the disk due to the temperature rise determined using the methodology in Section II E. The fly height prediction can be improved by incorporating electrostatic forces in the HDI[38].

## V. CONCLUSION

We have introduced a numerical model to predict the slider temperature profile and the fly height for a flying TFC slider over a rotating disk. Next, we compared our simulation results with touchdown experiments performed with a magnetic recording head flying over a rotating Al-Mg disk. Our model considers the effects of disk temperature rise, asperity-based adhesion and contact forces, combined heat transfer due to air conduction & phonon conduction and friction heating to accurately predict the fly height and heat transfer at near-contact. The heat transfer coefficient due to wave-based phonon conduction theory is determined as function of the spacing, the disk surface temperature and the slider-disk surface temperature difference, accounting for the effect of DLC layers on the slider/disk and magnetic layers on the disk.

Initially, the ECS temperature increases with increasing TFC power due to larger joule heating generated at the higher TFC power. However, as the flying head approaches the rotating disk with a further increase in TFC power, enhanced nanoscale heat transfer due to air conduction and phonon conduction leads to a drop in the ECS temperature change vs. the TFC power curve until touchdown. Beyond touchdown, the ECS temperature increases again with increasing TFC power. Our results show that the simulation without the disk temperature model overestimates the ECS cooling drop compared to the simulation with the disk temperature model. The incorporation of adhesion force between the head and the disk causes a reduction in the fly height, leading to a steeper ECS cooling drop than the simulation without adhesion force. The simulation with phonon conduction shows a larger ECS cooling drop compared to the simulation without phonon conduction. The simulation with friction heating predicts a larger ECS temperature and a larger slope of ECS temperature vs. TFC power beyond contact. The simulation with disk temperature model, air & phonon conduction, adhesion & contact forces and friction heating agrees well with the experiment at different rotational speeds (5400 RPM, 7200 RPM).

## ACKNOWLEDGMENTS

The data that support the findings of this study are available from the corresponding author upon reasonable request. This

project was supported by the Computer Mechanics Laboratory (CML) at the University of California, Berkeley and funded by the Advanced Storage Research Consortium (ASRC). We thank Yuan Ma of Texas A&M University, Robert Smith, JP Peng, Weidong Huang, Erhard Schreck, Sukumar Rajauria, Tan Trinh and Qing Dai of Western Digital and Huan Tang of Seagate for supplying components and helpful discussions.

[1]M. Kurita, J. Xu, M. Tokuyama, K. Nakamoto, S. Saegusa, and Y. Maruyama, IEEE Trans. Magn. **41**, 3007 (2005).
[2]J.-Y. Juang, D. Chen, and D. B. Bogy, IEEE Trans. Magn. **42**, 241 (2006).
[3]K. Aoki and T. Watanabe, IEEE Trans. Magn. **45**, 816 (2009).
[4]H. Zheng, H. Li, and F. E. Talke, IEEE Trans. Magn. **45**, 3628 (2009).
[5]N. Liu, J. Zheng, and D. B. Bogy, J. Appl. Phys. **108**, 016102 (2010).
[6]L. Li, H. Zheng, and F. E. Talke, Tibol. Lett. **59**, 12 (2015).
[7]J. Xu, Y. Shimizu, M. Furukawa, J. Li, Y. Sano, T. Shiramatsu, Y. Aoki, H. Matsumoto, K. Kuroki, and H. Kohira, IEEE Trans. Magn. **50**, 114 (2014).
[8]H. Wu, S. Xiong, S. Canchi, E. Schreck, and D. Bogy, Appl. Phys. Lett. **108**, 093106 (2016).
[9]Y. Ma, A. Ghafari, B. Budaev, and D. Bogy, Appl. Phys. Lett. **108**, 213105 (2016).
[10]H. Wu and D. Bogy, Appl. Phys. Lett. **110**, 033104 (2017).
[11]J. Zheng, Y.-K. Chen, and Q. Zhou, Sci. Rep. **8**, 3343 (2018).
[12]N. Zuckerman, J. D. Kiely, M. C. Anaya-Dufresne, M. T. Johnson, and R. M. Crone, IEEE Trans. Magn. **55**, 3300205 (2019).
[13]S. Sakhalkar, Q. Cheng, A. Ghafari, Y. Ma, and D. Bogy, Appl. Phys. Lett. **115**, 223102 (2019).
[14]J.-G. Zhu, X. Zhu, and Y. Tang, IEEE Trans. Magn. **44**, 125 (2008).
[15]M. H. Kryder, E. C. Gage, T. W. McDaniel, W. A. Challener, R. E. Rottmayer, G. Ju, Y.-T. Hsia, and M. F. Erden, Proc. IEEE **96**, 1810 (2008).
[16]S. Sakhalkar and D. Bogy, Tribol. Lett. **65**, 166 (2017).
[17]S. Sakhalkar and D. Bogy, Tribol. Lett. **66**, 145 (2018).
[18]S. Sakhalkar and D. Bogy, IEEE Trans. Magn. **55**, 3300506 (2019).
[19]J. Kiely, P. Jones, Y. Yang, J. Brand, M. Anaya-Dufresne, P. Fletcher, F. Zavaliche, Y. Toivola, J. Duda, and M. Johnson, IEEE Trans. Magn. **53**, 3300307 (2017).
[20]S. Xiong, N. Wang, R. Smith, D. Li, E. Schreck, and Q. Dai, Tribol. Lett. **65**, 74 (2017).
[21]C. Boone, J. Li, I. Nunokawa, E. Schreck, M. Sugiyama, I. Tagawa, and Y. Udo, *US Patent 8995088B1 (31 March 2015)*.
[22]S. Zhang and D. Bogy, Int. J. Heat Mass Transf. **42**, 1791 (1999).
[23]D. Chen, N. Liu, and D. Bogy, J. Appl. Phys. **105**, 084303 (2009).
[24]B. Budaev and D. Bogy, Appl. Phys. Lett. **104**, 061109 (2014).
[25]B. Budaev and D. Bogy, J. Appl. Phys. **117**, 104512 (2015).
[26]B. Budaev, A. Ghafari, and D. Bogy, J. Appl. Phys. **119**, 144501 (2016).
[27]B. Budaev and D. Bogy, Appl. Phys. Lett. **109**, 231905 (2016).
[28]B. Budaev and D. Bogy, Proc. R. Soc. A **473**, 20160584 (2017).
[29]B. Budaev and D. Bogy, Z. Angew. Math. Phys. **69**, 71 (2018).
[30]S. Shen, A. Narayanaswamy, and G. Chen, Nano Lett. **9**, 2909 (2009).
[31]K. Kim, B. Song, V. Fernndez-Hurtado, W. Lee, W. Jeong, L. Cui, D. Thompson, J. Feist, M. T. H. Reid, F. J. Garca-Vidal, J. C. Cuevas, E. Meyhofer, and P. Reddy, Nature **528**, 387 (2015).
[32]R. Prasher, Appl. Phys. Lett. **94**, 041905 (2009).
[33]M. Prunnila and J. Meltaus, Phys. Rev. Lett. **105**, 125501 (2010).
[34]Y. Ezzahri and K. Joulain, Phys. Rev. B **90**, 115433 (2014).
[35]C. Henkel and P. P. Schmidt, J. Opt. Soc. Am. B **36**, C10 (2019).
[36]H. Stanley, I. Etsion, and D. Bogy, Trans. ASME **112**, 98 (1990).
[37]J. Zheng and D. Bogy, Tribol. Lett. **38**, 283 (2010).
[38]J. Zheng and D. Bogy, IEEE Trans. Magn. **48**, 2415 (2012).
[39]J. Zheng and D. Bogy, Microsyst. Technol. **19**, 1377 (2013).
[40]G.-J. Lo, C. M. Mate, and Q. Dai, Tribol. Lett. **64**, 6 (2016).
[41]S. Lee, C.-D. Yeo, D. Purani, and A. S. Kim, IEEE Trans. Magn. **50**, 3300307 (2014).
[42]K. Ono, ASME Journal of Tribology **134**, 011402 (2012).
[43]K. Ono, IEEE Trans. Magn. **53**, 3300806 (2017).
[44]K. Ono, ASME Journal of Tribology **139**, 062001 (2017).
[45]A. Y. Suh and A. A. Polycarpou, J. Appl. Phys. **97**, 104328 (2005).
[46]A. Y. Suh and A. A. Polycarpou, J. Appl. Phys. **99**, 08N111 (2006).
[47]C. T. Rettner, IEEE Trans. Magn. **34**, 2387 (1998).
[48]W. Zhou, B. Liu, S. Yu, and W. Hua, Jpn. J. Appl. Phys. **49**, 095206 (2010).
[49]S. Zhang, *Numerical Investigations of Particle Contamination and Thermal Effects in a Slider Disk Interface*, Ph.D. thesis, University of California, Berkeley (1997).
[50]L. M. Martyushev and V. D. Seleznev, Phys. Rep. **426**, 1 (2006).
[51]C. M. Mate, R. Payne, Q. Dai, and K. Ono, Phys. Rev. Lett. **97**, 216104 (2006).
[52]J. Dahl and D. B. Bogy, Tribol Lett. **54**, 35 (2014).
[53]B. Bhushan, "Modern tribology handbook," (CRC Press, Boca Raton, FL, 2000) Chap. 6, pp. 235–272, 1st ed.
[54]F. Ling, W. Lai, and D. Lucca, "Fundamentals of surface mechanics," (Springer, New York, 2002) Chap. 2, pp. 11–68, 2nd ed.
[55]A. Ovcharenko, M. Yang, K. Chun, and F. E. Talke, IEEE Trans. Magn. **46**, 770 (2010).
[56]S. Lu, *Numerical simulation of slider air bearings*, Ph.D. thesis, University of California, Berkeley (1997).
[57]J. Zheng, *Dynamics and Stability of Thermal Flying-height Control Sliders in Hard Disk Drives*, Ph.D. thesis, University of California, Berkeley (2012).
[58]M. G. Beghi, A. C. Ferrari, K. B. K. Teo, J. Robertson, C. E. Bottani, A. Libassi, and B. K. Tanner, Appl. Phys. Lett. **81**, 38044 (2002).
[59]M. Shamsa, W. L. Liu, A. A. Balandin, C. Casiraghi, W. I. Milne, and A. C. Ferrari, Appl. Phys. Lett. **89**, 161921 (2006).
[60]V. Gupta and D. Bogy, IEEE Trans. Magn. **41**, 610 (2005).
[61]S. Canchi and D. Bogy, IEEE Trans. Magn. **46**, 764 (2010).
[62]Y.-K. Chen, J. Zheng, and D. Bogy, Appl. Phys. Lett. **100**, 243104 (2012).
[63]Y.-K. Chen, J.-P. Peng, and D. Bogy, IEEE Trans. Magn. **50**, 3301707 (2014).
[64]H.-K. Lyeo and D. G. Cahill, Phys. Rev. B **73**, 144301 (2006).
[65]P. E. Hopkins, ISRN Mech. Eng. **2013**, 682586 (2013).
[66]Y. Ma, W. D. Zhou, S. K. Yu, and W. Hua, Tibol. Lett. **56**, 93 (2014).